

Magnetization reversal through an antiferromagnetic state

S. Ghara,^{1,*} E. Barts,² K. Vasin,^{1,3} D. Kamenskyi,¹ L. Prodan,¹
V. Tsurkan,^{1,4} I. Kézsmárki,¹ M. Mostovoy,² and J. Deisenhofer¹

¹*Experimentalphysik V, Center for Electronic Correlations and Magnetism,
Institute for Physics, University of Augsburg, D-86135 Augsburg, Germany*

²*Zernike Institute for Advanced Materials, University of Groningen,
Nijenborgh 4, 9747 AG Groningen, The Netherlands*

³*Institute for Physics, Kazan (Volga region) Federal University, 420008 Kazan, Russia*

⁴*Institute of Applied Physics, MD-2028 Chişinău, Republic of Moldova*

Magnetization reversal in ferro- and ferrimagnets is a well-known archetype of non-equilibrium processes, where the volume fractions of the oppositely magnetized domains vary and perfectly compensate each other at the coercive magnetic field. Here, we report on a fundamentally new pathway for magnetization reversal that is mediated by an antiferromagnetic state. Consequently, an atomic-scale compensation of the magnetization is realized at the coercive field, instead of the mesoscopic or macroscopic domain cancellation in canonical reversal processes. We demonstrate this unusual magnetization reversal on the Zn-doped polar magnet $\text{Fe}_2\text{Mo}_3\text{O}_8$. Hidden behind the conventional ferrimagnetic hysteresis loop, the surprising emergence of the antiferromagnetic phase at the coercive fields is disclosed by a sharp peak in the field-dependence of the electric polarization. In addition, at the magnetization reversal our THz spectroscopy studies reveal the reappearance of the magnon mode that is only present in the pristine antiferromagnetic state. According to our microscopic calculations, this unusual process is governed by the dominant intralayer coupling, strong easy-axis anisotropy and spin fluctuations, which result in a complex interplay between the ferrimagnetic and antiferromagnetic phases. Such antiferro-state-mediated reversal processes offer novel concepts for magnetization control, and may also emerge for other ferroic orders.

Magnetization reversal processes in ferro- and ferrimagnets are essential in many of their applications. The on-demand control of domains upon magnetization reversal is a hotbed of new developments for spintronics¹⁻⁴. The mutual coupling of magnetization and polarization in multiferroic materials can be exploited to reverse magnetization by electric field and for electric read-out of the magnetic state^{5,6}. In this paper we report an unconventional magnetization reversal observed in the field-induced ferrimagnetic (FiM) state of lightly Zn doped $\text{Fe}_2\text{Mo}_3\text{O}_8$. We find that reversing the magnetization requires the resurrection of the antiferromagnetic (AFM) state, which is evidenced by an increase of the static polarization and the reemergence of a THz excitation characteristic of the AFM state. Our theoretical calculations show that the spin ordering in $\text{Fe}_2\text{Mo}_3\text{O}_8$ is strongly affected by the presence of two magnetic Fe sites with different magnetic moments and magnitudes of magnetic anisotropy. In combination with a strong intralayer and a weak interlayer exchange coupling of the honeycomb layers the remarkable magnetization reversal through the AFM state in $\text{Fe}_{2-x}\text{Zn}_x\text{Mo}_3\text{O}_8$ with $x = 0.14$ can be reproduced by our simulations.

Recently, the honeycomb antiferromagnets $A_2\text{Mo}_3\text{O}_8$ ($A=\text{Mn,Fe,Co,Ni,Zn}$) have emerged as a versatile material class with a hexagonal structure in the polar space group $P6_3mc$ ⁷⁻¹⁵. These compounds exhibit optical magnetoelectric effects such as directional dichroism^{16,17} and giant thermal Hall effects^{18,19}, and the control of

magnetization and polarization can be achieved in magnetic fields of a few Tesla^{20,21} or even by ultrafast modulation via laser pulses²². Particular attention has been drawn to $\text{Fe}_2\text{Mo}_3\text{O}_8$ with a Néel temperature $T_N=60$ K, below which a collinear AFM spin order of the magnetic Fe^{2+} ions coaligns with the polarization along the crystallographic c -axis as shown in Fig. 1a. The Fe^{2+} ions occupy tetrahedrally coordinated sites (A-site) and octahedrally coordinated ones (B-site). Within each of the hexagonal layers (Fig. 1c) the inequality of the orbital contributions to the magnetic moments of A- and B-site ions with spin $S = 2$ results in finite magnetizations $\mathbf{M}_{1,2}$ of each layer with opposite sign for adjacent layers (green arrows in Fig. 1a). Such an AFM spin configuration can be characterized by the AFM Néel vectors for each sublattice of Fe^{2+} , e.g. $\mathbf{L}_A = \frac{1}{2}(\mathbf{M}_{1A} - \mathbf{M}_{2A})$ with sublattice magnetizations \mathbf{M}_{1A} and \mathbf{M}_{2A} for the two different A-sites. The AFM order parameter is then given by $\mathbf{L} = \mathbf{L}_A + \mathbf{L}_B = \frac{1}{2}(\mathbf{M}_1 - \mathbf{M}_2)$. Upon application of a magnetic field along the c -axis, a transition to a FiM phase occurs, where the two anti-aligned sublattices are formed by A-site and B-site ions, respectively, corresponding to a flip of the layer magnetization in every second layer, as shown in Fig. 1b^{20,21}. This complies with a clearly dominating AFM intralayer exchange coupling J_{\parallel} (Fig. 1c) in comparison with the weaker interlayer couplings J_{AA} and J_{BB} (Fig. 1d). The order parameter of the FiM state can be expressed as the sum of the two sublattice contributions $\mathbf{M}_{A,B}$ or of the layer magnetizations $\mathbf{M}_{1,2}$ as $\mathbf{M} = \mathbf{M}_A + \mathbf{M}_B = \mathbf{M}_1 + \mathbf{M}_2$.

The FiM state was shown to exhibit a linear magnetoelectric effect²¹ and can be stabilized by substituting Fe

* somnath.ghara@physik.uni-augsburg.de

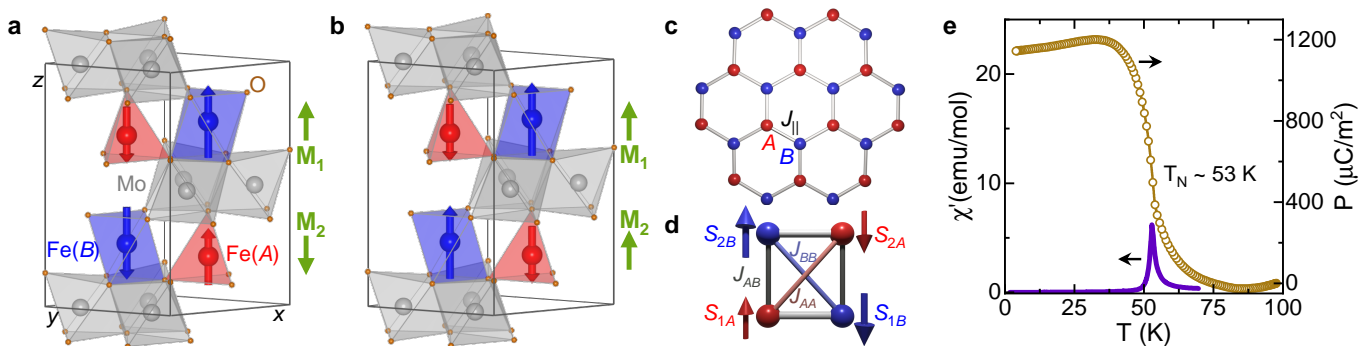


FIG. 1. | **Crystal structure and magnetic order in $\text{Fe}_{2-x}\text{Zn}_x\text{Mo}_3\text{O}_8$.** **a, b**, Unit cell of $\text{Fe}_2\text{Mo}_3\text{O}_8$ in the AFM state and the FiM state, with tetrahedral (*A*) and octahedral (*B*) sites shown in red and blue, respectively. The green arrows indicate the overall magnetization of each layer. **c**, Hexagonal layer formed by the Fe sites with dominant AFM exchange coupling J_{\parallel} . **d**, Exchange couplings J_{AA} , J_{BB} and J_{AB} between the Fe ions at *A* and *B* sites of adjacent layers in the AFM state. **e**, Temperature dependence of the real part of the magnetic *ac* susceptibility χ' (solid line) and polarization *P* (open symbols) in $\text{Fe}_{1.86}\text{Zn}_{0.14}\text{Mo}_3\text{O}_8$.

by non-magnetic Zn, which preferably occupies the tetrahedral A-sites^{8,9,21,23,24}. The persistence of the field-induced FiM state in Zn-doped $\text{Fe}_2\text{Mo}_3\text{O}_8$ upon decreasing and reversing the field was reported beforehand^{21,25}, but the origin of this metastable state has not been addressed previously. The Néel temperature in the system $\text{Fe}_{1.86}\text{Zn}_{0.14}\text{Mo}_3\text{O}_8$ is reduced to 53 K as indicated by the peak in the magnetic susceptibility shown in Fig. 1e, while the polarization shows an increase at the magnetic ordering and saturation-like behavior in the AFM phase comparable to pure $\text{Fe}_2\text{Mo}_3\text{O}_8$ ²¹. The FiM state at this Zn concentration persists as a metastable state in zero magnetic field below about 40 K, i.e. the remanent magnetization during hysteretic cycling remains finite, as seen in Figs. 2a and 2b²⁵. By comparing the hysteretic cycle of magnetization and polarization measurements in external magnetic fields in this temperature range, we find a strong increase in polarization, whenever the magnetization changes sign in the vicinity of the coercive fields. We ascribe this increase in polarization to the reoccurrence of the AFM ground state, which has a larger polarization than the FiM state^{20,21}, during the magnetization reversal of the FiM state. This assignment is supported by the reoccurrence of the characteristic low-energy THz excitation of the AFM phase in the same field range. Our microscopic theoretical approach can explain the origin of the FiM metastable state and the resurrection of the AFM phase upon magnetization reversal.

An unusual magnetization reversal

In this section, we discuss how the reoccurrence of the AFM state at the magnetization reversal is reflected in the polarization. In Figs. 2a and 2b we show the magnetization $M(H)$ (dashed lines) and polarization $P(H)$ (solid lines) measured as a function of the external magnetic field along the *c*-axis at $T = 20$ K and $T = 13$ K, respectively. The magnetization curves starting at zero

magnetic field (black dashed lines) in the pristine AFM state show a transition to the FiM state in the shaded field range, and upon reversing the magnetic field, a typical FiM-like hysteresis shows up with coercive fields of the order of the critical fields of the AFM-to-FiM transition. This is in agreement with previously reported data²⁵ and samples with similar Zn concentrations²¹. The polarization shows a strong decrease upon the transition from the AFM to the FiM state, and a linear magnetoelectric effect occurs in the FiM state (shown clearly in Supplementary Fig. 1), both observations in line with literature²¹. Intriguingly, whenever the magnetization starts to deviate from its saturation values $\pm M_S$ during the cycling, a strong increase in polarization occurs, reaching its maximum at the coercive field (see e.g. shaded area in Fig. 2a). Such an unusual behavior has not been observed beforehand in Zn-doped $\text{Fe}_2\text{Mo}_3\text{O}_8$ or other FiM multiferroics exhibiting a linear magnetoelectric effect²⁶.

It is important to note that both the critical and coercive fields and the peak height of the polarization depend on temperature, as can be seen by the comparison of Figs. 2a and 2b. At 20 K the maximal value of the polarization at the coercive field is about half of the one in the pristine AFM phase (Fig. 2a), but at 13 K the value is already considerably reduced. At 30 K the maximal polarization value at the coercive field almost reaches the value of the pristine AFM phase (see Supplementary Fig. 2). We regard this as evidence that in the vicinity of the coercive fields, when the monodomain FiM phase usually turns to an equal share of up and down domains with volume fractions $x_{\text{fim}\uparrow}(H, T)$ and $x_{\text{fim}\downarrow}(H, T)$, respectively, a significant fraction of the sample volume, denoted as $x_{\text{afm}}(H, T)$, exhibits the properties of the pristine AFM state with high polarization values. The AFM fraction assisting the magnetization reversal emerges now as a metastable state. Consequently, we analyze the magnetic-field dependent magnetization and polarization data assuming that the en-

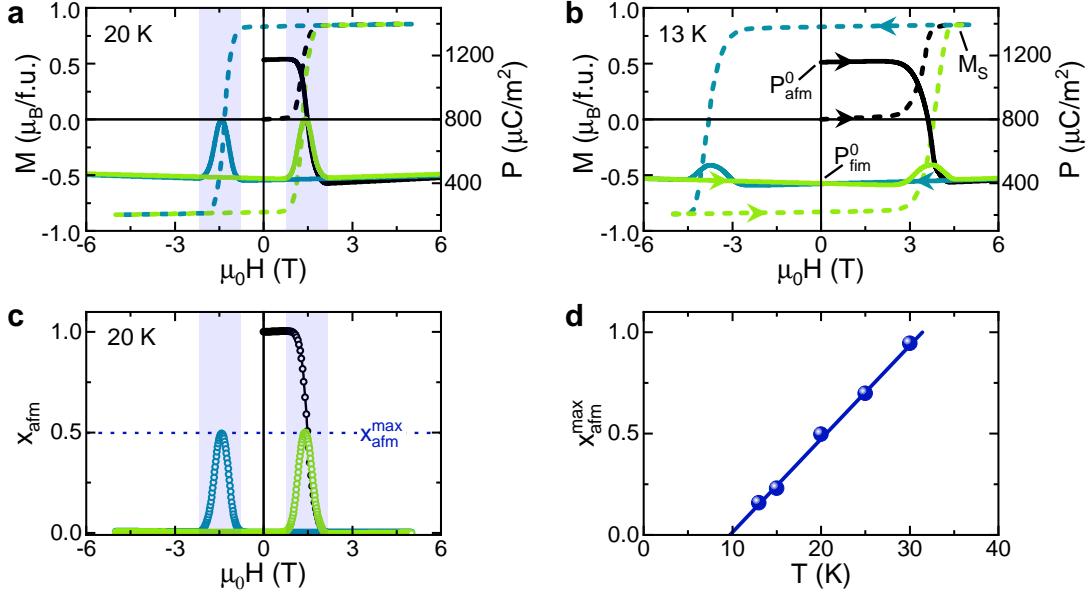


FIG. 2. | **Signatures of the resurrection of the AFM state in magnetization and polarization.** **a,b**, Magnetic field-dependent magnetization M (dashed lines) and polarization P (solid lines) along the c axis at 20 K and 13 K, respectively. **c**, Magnetic field-dependent antiferromagnetic volume fraction (x_{afm}) at 20 K extracted from magnetization and polarization data using Eq. (2). The vertical shading in **a** and **c** indicates the field range, where the pristine AFM state reappears upon magnetization reversal. **d**, Temperature dependence of the maximum values of x_{afm} . The solid line is a guide to the eye.

tire sample volume is distributed between three fractions only, i.e. $x_{\text{afm}} + x_{\text{fim}\uparrow} + x_{\text{fim}\downarrow} = 1$. The magnetization is then solely determined by the FiM volume fractions as $M(H) = M_S(x_{\text{fim}\uparrow} - x_{\text{fim}\downarrow})$, while the polarization bears the contribution of all three magnetic volume fractions,

$$P(H) = x_{\text{afm}}P_{\text{afm}}^0 + P_{\text{fim}}^0(x_{\text{fim}\uparrow} + x_{\text{fim}\downarrow}) + \alpha H \frac{M(H)}{M_S}. \quad (1)$$

Here, P_{afm}^0 denotes the polarization of the pristine anti-ferromagnet in zero magnetic field, P_{fim}^0 the corresponding polarization of the FiM phase upon lowering the field to zero after reaching the mono-domain FiM states with $M(H) = \pm M_S$ (see Fig. 2b). The only parameter, which had to be determined by fitting the $P(H)$ curves, is the magnetoelectric susceptibility coefficient α , which was derived in the corresponding linear regimes (a possible contribution $\propto H^2$ was found to be negligible, see Supplementary note 1). With this approach we extracted the AFM volume fraction given by,

$$x_{\text{afm}}(H) = \frac{1}{P_{\text{afm}}^0 - P_{\text{fim}}^0} \left[P(H) - P_{\text{fim}}^0 - \alpha H \frac{M(H)}{M_S} \right]. \quad (2)$$

The result for $T = 20$ K is shown in Fig. 2c. The values of $x_{\text{afm}}(H)$ yield symmetric peaks centered at the coercive fields. The corresponding maximum values $x_{\text{afm}}^{\text{max}}$ are shown in Fig. 2d for all investigated temperatures. It decreases linearly with decreasing temperature and extrapolates to zero at around 10 K. This is in agreement with the absence of any macroscopic polarization peak at the magnetization reversal below 10 K.

To corroborate the above scenario derived from dc magnetization and polarization measurements, we will discuss in the following the dynamic fingerprints of the magnetic volume fractions in the THz frequency regime.

Probing magnetic phases via THz spectroscopy

The resurrection of the pristine AFM phase and its coexistence with the FiM fraction upon magnetization reversal can also be revealed in the THz spectra by investigating the field evolution of the characteristic elementary excitations of the two magnetic phases, which were previously identified²⁵. In Fig. 3b we show the THz absorption spectra (red colors) at 25 K for light polarisation $E^\omega \parallel a$ for several magnetic fields during the virgin magnetization curve with the external magnetic field $H \parallel c$ as indicated by the same colors in the M - H -diagram in Fig. 3a. The spectrum of the AFM ground state at zero field and the one of the saturated FiM state in a field of 2 T serve as benchmarks for the virgin AFM and mono-domain FiM states with $x_{\text{afm}} = 1$ and $x_{\text{fim}\uparrow} = 1$, respectively. The absorption spectra shown in Fig. 3c correspond to reversed magnetic fields of the hysteric cycle (green curves) and show the evolution of the magnetic phases upon approaching the magnetization reversal at about -1 T and reaching again a fully saturated FiM state at -2 T with $x_{\text{fim}\downarrow} = 1$. The spectrum of the pristine AFM state is characterized by one distinct spectral feature in this configuration - the narrow electric-dipole active absorption mode at 44 cm^{-1} (AFM mode) shown in Fig. 3b, which was identified previously as a clear fingerprint of the AFM state both in pure $\text{Fe}_2\text{Mo}_3\text{O}_8$ ²⁷ and

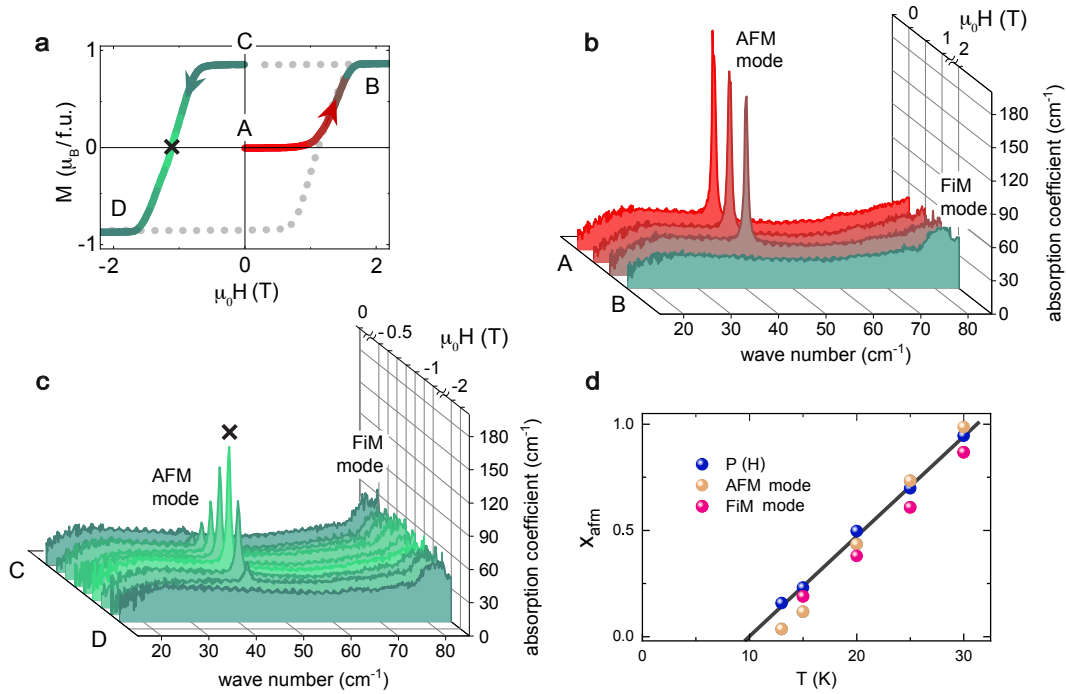


FIG. 3. | **Demonstration of the reappearance of the AFM state upon magnetization reversal via THz spectroscopy.** **a**, Magnetic field-dependent magnetization $M(H)$ at 25 K. Selected segments (A-B and C-D) of the magnetization curve are highlighted by colors to indicate the field regions of the THz data shown in **b** and **c**. **b**, THz absorption spectra at 25 K recorded at different magnetic fields ($H \parallel c$) ranging between the segment A-B of panel **a**. **c**, THz absorption spectra recorded at different magnetic fields ranging between the segment C-D of panel **a**. The THz spectrum indicated by the symbol \times is recorded at the coercive field (see panel **a**). **d**, Temperature dependence of the maximum values of x_{afm} at the magnetization reversal obtained directly from the integrated intensity of the AFM mode and the FiM mode (via $1 - x_{\text{fim}}$). For comparison, x_{afm} values obtained from the polarization analysis are reproduced in **d**. The solid line is a guide to the eye.

in $\text{Fe}_{1.86}\text{Zn}_{0.14}\text{Mo}_3\text{O}_8$ ²⁵. The mode at 44 cm^{-1} is clearly absent in the spectra of the saturated FiM states for $H = \pm 2 \text{ T}$, where only one excitation at about 83 cm^{-1} (FiM mode) is observed as a characteristic fingerprint of the FiM state²⁵.

Upon lowering and reversing the external magnetic field from the saturated FiM state at 2 T no significant changes in the absorption spectra occur as long as the condition $M(H) = M_S$ holds (spectra not shown). Intriguingly, on approaching magnetization reversal an excitation at the eigenfrequency of the characteristic AFM mode at 44 cm^{-1} emerges, reaches a maximum in intensity at around $H_c = -1 \text{ T}$, and decreases in intensity again for $|H| > H_c$ as shown in Fig. 3c. Finally, the mode disappears again when reaching magnetization saturation with $M(H) = -M_S$ on approaching a field of -2 T . Based on the comparison with the properties of the spectrum in the pristine AFM state, we identify this emerging mode with the AFM mode: eigenfrequency and linewidth of the two modes coincide and they obey the same electric-dipole selection rule $E^\omega \parallel a$ (see Supplementary Fig 3). In addition, the intensity of the FiM mode clearly decreases with increasing intensity of AFM mode during magnetization reversal, showing that the

THz spectra provide direct information on the coexistence of the AFM and FiM states in this magnetic field range.

We used the integrated intensities of AFM and FiM modes for all spectra to extract the AFM volume fraction x_{afm} and the FiM one x_{fim} by normalizing the intensity values to the intensity of the modes in the pristine AFM and the saturated FiM states, respectively (see Supplementary note 2 for details). Note that our THz probe does not distinguish up and down FiM states, therefore $x_{\text{fim}} = x_{\text{fim}\uparrow} + x_{\text{fim}\downarrow}$. The values of x_{afm} obtained directly from the AFM mode and using $x_{\text{afm}} = 1 - x_{\text{fim}}$ from the FiM mode are shown in Fig. 3d for all measured temperatures, together with the values of x_{afm} from the above analysis of the magnetization and polarization using Eq. (2). The agreement of the x_{afm} values from the dynamic THz probe and the static polarization and magnetization values is very good and confirms the unusual resurrection of the AFM ground state as a metastable state during the magnetization reversal of the FiM state.

Having established the magnetization reversal through the AFM state using our experimental observations, we will now discuss a theoretical approach that explains this scenario from a microscopic point of view.

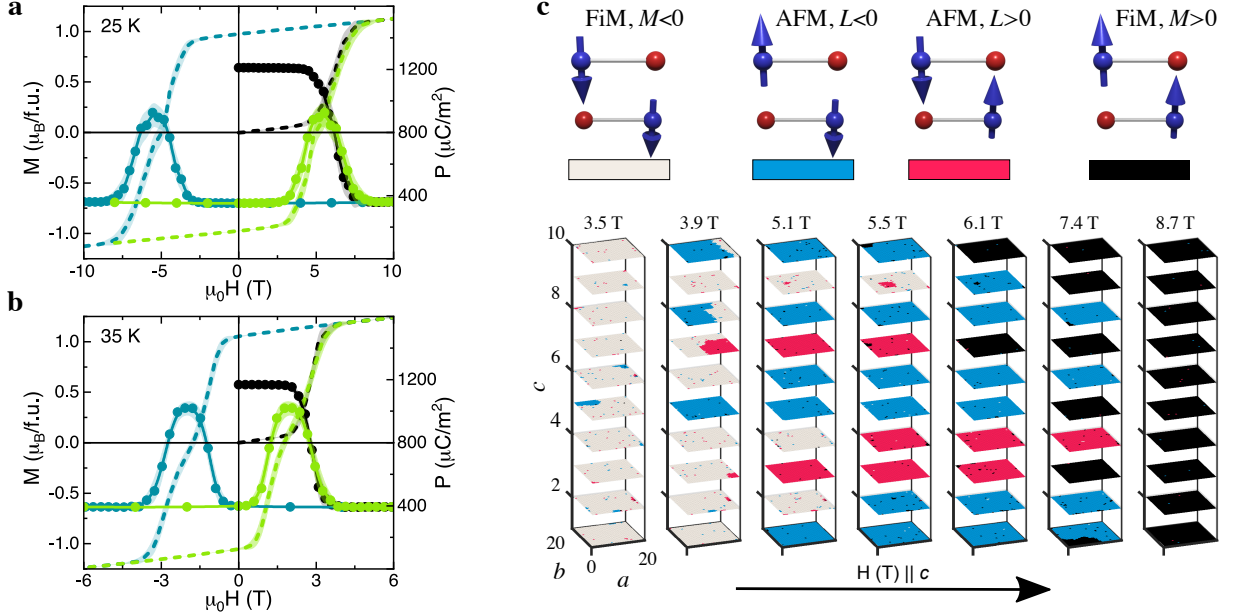


FIG. 4. | **Simulation of spin-state evolution upon magnetization reversal.** **a,b**, Magnetic field dependence of calculated magnetization M (dashed lines) and polarization P (solid circles) at 25 K and 35 K, respectively. **c**, Snapshots of spin configurations at different magnetic fields at 25 K during a magnetization reversal process from a FiM down-domain state to a FiM up-domain state. Each plaquette corresponds to a unit cell of $\text{Fe}_{1.86}\text{Zn}_{0.14}\text{Mo}_3\text{O}_8$, with $M = -1, L = 0$ (white), $M = 0, L = -1$ (blue), $M = 0, L = +1$ (red) and $M = +1, L = 0$ (black), where the AFM order parameter $L = (S_1 - S_2)/2$ and the FiM order parameter $M = (S_1 + S_2)/2$ are determined by the B -site spins $S_{1,2}$ in the unit cell. Color coding of magnetic orders is shown at the top of the panel. The planes are ab layers stacked along the c axis.

Microscopic theory of the magnetization reversal

In order to understand the puzzling appearance of the AFM phase with its high polarization at magnetization reversals, we consider the following spin model

$$E = J_{\parallel} \sum_{\langle i,j \rangle} s_i \sigma_j + J_{\perp} \sum_{i \in A} s_i (\sigma_{i+c/2} + \sigma_{i-c/2}) - H \left(\sum_{i \in A} m_A s_i + \sum_{j \in B} m_B \sigma_j \right), \quad (3)$$

where $s_i = S_i^z/S$ with $S_i^z = 0, \pm 1, \pm 2$ denoting the c -axis projection of the spin of a tetrahedrally coordinated Fe^{2+} ion ($S = 2$) on sublattice A, and $\sigma_j = \pm 1$ is an Ising variable describing the strongly anisotropic spins on sublattice B of octahedrally coordinated Fe ions. The first term in Eq. (3) describes the dominating AFM exchange interaction $J_{\parallel} > 0$ between neighboring spins in the ab -layers (see Fig. 1c) and the second term describes the weak effective ferromagnetic interaction $J_{\perp} < 0$ between spins in neighboring layers along the vertical AB bonds, resulting from the interplay between the three AFM interlayer interactions J_{AA} , J_{BB} and J_{AB} ²⁸ depicted in Fig. 1d. Here, $\sigma_{i \pm c/2}$ denotes the B-spins located above and below the spin on the A-site i . The last term is the Zeeman energy for a magnetic field applied along the c axis with the magnetic moments of A and B site spins set to $m_B = 4.5 \mu_B$ and $m_A = 4.2 \mu_B$. These values are in

agreement with neutron diffraction measurements⁹ and reproduce the experimentally observed saturation magnetization $M_s = 0.86 \mu_B$ per f.u. for $x = 0.14$ at low temperature assuming that Zn substitutes Fe on tetrahedral sites^{8,9,21,24}. The large deviation of m_B from the spin-only value $4 \mu_B$ results from the unquenched orbital moment of Fe^{2+} ions on octahedral sites, which also leads to strong single-ion anisotropy along the c axis and allows us to describe B-spins by Ising variables. The relatively weak anisotropy of the A-site ions is neglected.

With this approach we first simulate the temperature and magnetic field dependence of the magnetization and polarization in pure $\text{Fe}_2\text{Mo}_3\text{O}_8$ showing the field-induced transition from the AFM to the FiM state (see Supplementary notes 3 & 4 for details of calculations). Supplementary Fig. 4a shows $M(H)$ curves calculated for $J_{\parallel} = 47 \text{ K}$, $J_{\perp} = -1.2 \text{ K}$, which are in quantitative agreement with experiment^{20,21}. The magnetically-induced electric polarization (shown in Supplementary Fig. 4b) is calculated using a microscopic magnetoelectric coupling. The field-induced transition corresponds to a spin-flip transition instead of the spin-flop transition expected for isotropic spins. The net magnetic moment of an ab layer that governs this transition depends on temperature, because the isotropic A-site spins show larger thermal fluctuations than the Ising spins on B-sites. As a result, the net magnetic moment of an ab layer near T_N is larger than at low temperatures²¹. Conversely, the critical field nec-

essary to flip spins just below T_N is significantly smaller than that at low temperatures, which explains the dramatic increase of the spin-flip field upon decreasing temperature in pure $\text{Fe}_2\text{Mo}_3\text{O}_8$ ^{20,21}. The expansion of the boundary of the AFM phase towards higher magnetic fields at low temperatures plays an important role in the emergence of this phase at the magnetization reversals.

In Fig. 4 we show the main results of our calculations with regard to the experimentally observed polarization anomaly upon magnetization reversal in $\text{Fe}_{1.86}\text{Zn}_{0.14}\text{Mo}_3\text{O}_8$. Our theory reproduces the hysteretic magnetization and the polarization curves with a peak at the coercive field (Figs. 4a and 4b). As temperature decreases, the coercive field increases due to the reduction of thermal fluctuations. The substitution of nonmagnetic Zn for Fe on tetrahedral sites increases the net magnetic moment, which further stabilizes the FiM state reducing the critical field to 0 just below T_N at $x = 0.14$ ²⁵. To reproduce the strong reduction of the critical field upon doping, we use a much smaller value of the interlayer exchange constant, $J_\perp = -0.2\text{K}$. In fact, the effective ferromagnetic interaction J_\perp is expected to be x -dependent, as it results from the interplay between the three AFM interlayer interactions J_{AA} , J_{BB} and J_{AB} (as depicted in Fig. 1d)²⁸. This interplay sensitively depends on the removal of magnetic ions from A-sites. The much weaker interlayer exchange coupling J_\perp may be the reason why this phenomenon is so prominent in the present compound $\text{Fe}_{1.86}\text{Zn}_{0.14}\text{Mo}_3\text{O}_8$. Even though it has not been reported for other compositions in the $\text{Fe}_{2-x}\text{Zn}_x\text{Mo}_3\text{O}_8$ series²¹, the necessary J_\perp for this unusual magnetization reversal may be realized only in a limited range of Zn concentrations.

Figure 4c shows snapshots of the spin configurations during the simulated magnetization reversal that starts from a prepared FiM state with negative saturation magnetization, which remains negative up to +3.5 T. Each plane corresponds to two neighboring magnetic layers of $\text{Fe}_{1.86}\text{Zn}_{0.14}\text{Mo}_3\text{O}_8$ and the color denotes the local magnetic ordering in the B-site sublattice described by the calculated local order parameters $L = (S_{B1} - S_{B2})/2 = +1$, $M = (S_{B1} + S_{B2})/2 = 0$ (red), $L = -1, M = 0$ (blue), $L = 0, M = +1$ (black), and $L = 0, M = -1$ (white). The strong intralayer AFM coupling aligns the spins of the A and B sublattices opposite to each other. Therefore, we consider only the B-site sublattice order parameters here. Starting out from a FiM state with negative saturated magnetization (white planes) on the left, planes with non-zero AFM order parameter emerge with increasing field in the vicinity of the coercive field (blue and red planes) before the FiM state with positive magnetization (black planes) is reached at the highest fields. The nearly uniform color of each plane reflects strong spin correlations in the ab layers. These spin correlations suppress the growth of droplets with the opposite magnetization, which are induced by the magnetic field reversal. As a result, the emergence of the AFM phase is delayed up to the coercive field. The above calculations,

supporting nicely the experimental findings, provide the microscopic understanding of how the strong strong easy-axis anisotropy together with the strong intralayer and weak interlayer couplings causes the unusual reappearance of the AFM state at the magnetization reversal in $\text{Fe}_{1.86}\text{Zn}_{0.14}\text{Mo}_3\text{O}_8$.

Summary

To summarize, by independent measurements of polarization, magnetization and THz absorption, we discovered a highly unusual magnetization reversal process of the FiM state in Zn-doped $\text{Fe}_2\text{Mo}_3\text{O}_8$, which involves the reappearance of the AFM ground state as a metastable state during the reversal process. Our theoretical simulations nicely reproduce this finding, showing that an Ising-like anisotropy of the octahedrally coordinated Fe spins, small magnetic moment of FiM ab layers and weak interlayer interactions are the main ingredients for the emergence of these metastable spin configurations: The persistence of the FiM state in zero field and the reappearance of the AFM state at the coercive field.

Although Zn-doped $\text{Fe}_2\text{Mo}_3\text{O}_8$ has a unique combination of properties that slow down kinetics of transitions between the FiM and AFM phases and allow for electric detection of these states, the conditions for layer-wise magnetization switching via metastable spin states of distinct characters may be realized in other (quasi) 2D magnetic systems²⁹⁻³². At this point we want to stress the difference between the honeycomb antiferromagnets $A_2\text{Mo}_3\text{O}_8$ and the van der Waals magnets. In the latter systems, the coexistence of AFM and ferromagnetic states usually requires a complex material design using nanofabrication, such as mechanical twisting in CrI_3 ³, whereas the honeycomb antiferromagnets $A_2\text{Mo}_3\text{O}_8$ ($A=\text{Fe,Co,Mn,Ni,Zn}$) provide a versatile intrinsic toolbox for tuning and controlling different spin configurations through layer-by-layer switching. In fact, a special coexistence of collinear antiferromagnetism with canted ferrimagnetism on adjacent honeycomb layers was recently observed in high-magnetic fields³³. We believe that similar exotic switching processes, involving metastable states of distinct magnetic order, can be achieved in these compounds by other external stimuli like pressure, voltage or intense light-fields, which will allow to control the growth and decay rates of the spin states and open new pathways for spintronic applications.

METHODS

Synthesis

Polycrystalline $\text{Fe}_{2-x}\text{Zn}_x\text{Mo}_3\text{O}_8$ samples were prepared by repeated synthesis at 1000°C of binary oxides FeO (99.999%), MoO_2 (99%), and ZnO in evacuated quartz ampoules aiming for a concentration with $x = 0.2$. Single crystals were grown by the chemical transport reaction method at temperatures between 950 and 900°C . TeCl_4 was used as the source of the transport agent. Large single crystals up to 5 mm were obtained after 4 weeks of transport. The X-ray diffraction of the crushed single crystals revealed a single-phase composition with a hexagonal symmetry using space group $P6_3mc$ and a Zn content corresponding to $x \approx 0.14$. The obtained lattice constants are $a = b = 5.773(2)$ Å and $c = 10.017(2)$ Å²⁵.

THz spectroscopy

Temperature and magnetic field dependent time-domain THz spectroscopy measurements were performed on a plane-parallel ac -cut single crystal of $\text{Fe}_{1.86}\text{Zn}_{0.14}\text{Mo}_3\text{O}_8$. A Toptica TeraFlash time-domain THz spectrometer was used in combination with a superconducting magnet, which allows for measurements at temperatures down to 2K and in magnetic fields up to $\pm 7\text{T}$. Measurements were performed in Voigt transmission configuration with the magnetic field parallel to the c -axis.

Magnetization Measurements

dc magnetization measurements were carried out with a Magnetic Property Measurement System (5 T MPMS-SQUID, Quantum Design). The magnetic field was applied along the c direction of a hexagonal-shaped single crystal with clear top-bottom ab planes.

Polarization Measurements

Electric polarization was obtained by measuring pyroelectric/magnetoelectric current with a Keysight electrometer (model number B2987A). For accessing low temperature and high magnetic fields, a Physical Property Measurement System (9 T PPMS, Quantum Design) and an Oxford helium-flow cryostat ($+14\text{T}$) were used. The measurements were carried with a hexagonal-shaped single crystal, where electrical contacts were made on top-bottom ab planes by silver paint and the electric polarization along the c axis was probed. The crystal was mounted in PPMS/cryostat in such a way that the magnetic field could be applied along the c axis and the field was varied with a rate of 100Oe/sec . The magnetic field-dependent electric polarization was obtained by integrating the magnetoelectric current over measurement time.

Numerical Simulations

The sum over spin projections on tetrahedral sites, s_i , in Eq.(3) can be performed analytically, which leaves an effective model of Ising variables $\{\sigma_i\}$ (for more details see Supplementary materials). This effective model was used to calculate the magnetization and antiferromagnetic order parameter, as well as for simulations of hysteresis

loops. We assume that the isotropic spins on A-sites quickly reach thermal equilibrium with the neighboring B-site spins, whereas the dynamics of the Ising spins occurs on a longer time scale and can be described by the Glauber dynamics³⁴. To simulate hysteresis curves, we employ Glauber dynamics, a Markov chain Monte Carlo algorithm used to study non-equilibrium physics of Ising models. For each curve, the initial state is prepared with simulated annealing starting from a high-temperature ($T = 90\text{K}$) random state. At each magnetic field value, we performed 50 measurements with 10^7 Glauber steps in-between after the waiting time of $5 \cdot 10^8$ steps with no measurements. The total number of field points is 32. The results were averaged over 20-30 disorder realizations. Open boundary conditions in all three directions were used to speed up the magnetization reversal. The nonmagnetic Zn impurities were modeled by $S_i = 0$ on randomly chosen A-sites. We simulated the lattice of $20 \times 20 \times 20$ Ising spins.

DATA AVAILABILITY

The data that support the findings of this study are available from the corresponding author upon reasonable request.

ACKNOWLEDGEMENTS

This research was partly funded by Deutsche Forschungsgemeinschaft DFG via the Transregional Collaborative Research Center TRR 80 ‘‘From Electronic correlations to functionality’’ (Augsburg, Munich, Stuttgart). The support via the project ANCD 20.80009.5007.19 (Moldova) is also acknowledged. EB and MM acknowledge Vrije FOM-programma ‘Skyrmionics’ and the Peregrine high performance computing cluster.

AUTHOR CONTRIBUTIONS

L.P. and V.T. synthesized and characterized the crystals; S.G. and L.P. performed magnetization and polarization measurements and analyzed the data; D.K., K.V., and J.D. performed the THz measurements and analyzed the data; E.B. and M.M. performed the theoretical simulations; S.G., E.B., M.M., I.K., and J.D. wrote the manuscript; J.D. planned and coordinated the project. All authors contributed to the discussion and interpretation of the experimental and theoretical results and to the completion of the manuscript.

COMPETING INTERESTS

The authors declare that there are no competing interests.

-
- [1] Ostler, T. *et al.* Ultrafast heating as a sufficient stimulus for magnetization reversal in a ferrimagnet. *Nat. Commun.* **3**, 666 (2012).
- [2] Duine, R. A., Lee, K.-J., Parkin, S. S. P. & Stiles, M. D. Synthetic antiferromagnetic spintronics. *Nat. Phys.* **14**, 217–219 (2018).
- [3] Xu, Y. *et al.* Coexisting ferromagnetic–antiferromagnetic state in twisted bilayer CrI₃. *Nat. Nanotechnol.* **17**, 143–147 (2021).
- [4] Kim, S. K. *et al.* Ferrimagnetic spintronics. *Nature Mater.* **21**, 24–34 (2021).
- [5] Chai, Y. S. *et al.* Electrical control of large magnetization reversal in a helimagnet. *Nat Commun.* **5**, 4208 (2014).
- [6] Hassanpour, E. *et al.* Interconversion of multiferroic domains and domain walls. *Nat Commun.* **12**, 2755 (2021).
- [7] McCarroll, W. H., Katz, L. & Ward, R. Some ternary oxides of tetravalent molybdenum. *J. Am. Chem. Soc.* **79**, 5410–5414 (1957).
- [8] Varret, F., Czeskleba, H., Hartmann-Boutron, F. & Imbert, P. Étude par effet Mössbauer de l’ion Fe²⁺ en symétrie trigonale dans les composés du type (Fe, M)₂Mo₃O₈ (M = Mg, Zn, Mn, Co, Ni) et propriétés magnétiques de (Fe, Zn)₂Mo₃O₈. *J. Phys.* **33**, 549–564 (1972).
- [9] Bertrand, D. & Kerner-Czeskleba, H. Étude structurale et magnétique de molybdates d’éléments de transition. *J. Phys.* **36**, 379–390 (1975).
- [10] Le Page, Y. & Strobel, P. Structure of iron(II) molybdenum(IV) oxide Fe₂Mo₃O₈. *Acta Cryst. B* **38**, 1265–1267 (1982).
- [11] Strobel, P., Le Page, Y. & McAlister, S. P. Growth and physical properties of single crystals of Fe^{II}Mo₃^{IV}O₈. *J. Solid State Chem.* **42**, 242–250 (1982).
- [12] McAlister, S. P. & Strobel, P. Magnetic order in M₂Mo₃O₈ single crystals (M = Mn, Fe, Co, Ni). *J. Magn. Mater.* **30**, 340–348 (1983).
- [13] Abe, H., Sato, A., Tsujii, N., Furubayashi, T. & Shimoda, M. Structural refinement of T₂Mo₃O₈ (T = Mg, Co, Zn and Mn) and anomalous valence of trinuclear molybdenum clusters in Mn₂Mo₃O₈. *J. Solid State Chem.* **183**, 379–384 (2010).
- [14] Tang, Y. S. *et al.* Metamagnetic transitions and magnetoelectricity in the spin-1 honeycomb antiferromagnet Ni₂Mo₃O₈. *Phys. Rev. B* **103**, 014112 (2021).
- [15] Tang, Y. S. *et al.* Successive electric polarization transitions induced by high magnetic field in the single-crystal antiferromagnet Co₂Mo₃O₈. *Phys. Rev. B* **105**, 064108 (2022).
- [16] Yu, S. *et al.* High-temperature terahertz optical diode effect without magnetic order in polar FeZnMo₃O₈. *Phys. Rev. Lett.* **120**, 037601 (2018).
- [17] Reschke, S. *et al.* Confirming the trilinear form of the optical magnetoelectric effect in the polar honeycomb antiferromagnet Co₂Mo₃O₈. *npj Quantum Mater.* **7**, 1 (2022).
- [18] Ideue, T., Kurumaji, T., Ishiwata, S. & Tokura, Y. Giant thermal hall effect in multiferroics. *Nature Mater.* **16**, 797–802 (2017).
- [19] Park, S., Nagaosa, N. & Yang, B.-J. Thermal hall effect, spin nernst effect, and spin density induced by a thermal gradient in collinear ferrimagnets from magnon-phonon interaction. *Nano Lett.* **20**, 2741–2746 (2020).
- [20] Wang, Y. *et al.* Unveiling hidden ferrimagnetism and giant magnetoelectricity in polar magnet Fe₂Mo₃O₈. *Sci. Rep.* **5**, 12268 (2015).
- [21] Kurumaji, T., Ishiwata, S. & Tokura, Y. Doping-tunable ferrimagnetic phase with large linear magnetoelectric effect in a polar magnet Fe₂Mo₃O₈. *Phys. Rev. X* **5**, 031034 (2015).
- [22] Sheu, Y. M. *et al.* Picosecond Creation of Switchable Optomagnets from a Polar Antiferromagnet with Giant Photoinduced Kerr Rotations. *Phys. Rev. X* **9**, 031038 (2019).
- [23] Streltsov, S. V., Huang, D.-J., Solovyev, I. V. & Khomskii, D. I. Ordering of Fe and Zn Ions and the Magnetic Properties of FeZnMo₃O₈. *JETP Letters* **109**, 786–789 (2019).
- [24] Ji, Y. *et al.* Direct observation of preferential occupation of zinc ions in (Fe_{1-x}Zn_x)₂Mo₃O₈. *Solid State Commun.* **344**, 114666 (2022).
- [25] Csizi, B. *et al.* Magnetic and vibronic terahertz excitations in Zn-doped Fe₂Mo₃O₈. *Phys. Rev. B* **102**, 174407 (2020).
- [26] Arima, T. *et al.* Structural and magnetoelectric properties of Ga_{2-x}Fe_xO₃ single crystals grown by a floating-zone method. *Phys. Rev. B* **70**, 064426 (2004).
- [27] Kurumaji, T. *et al.* Electromagnon resonance in a collinear spin state of the polar antiferromagnet Fe₂Mo₃O₈. *Phys. Rev. B* **95**, 020405(R) (2017).
- [28] Solovyev, I. V. & Streltsov, S. V. Microscopic toy model for magnetoelectric effect in polar Fe₂Mo₃O₈. *Phys. Rev. Mater.* **3**, 114402 (2019).
- [29] Wu, H. C. *et al.* Anisotropic spin-flip-induced multiferroic behavior in kagome Cu₃Bi(SeO₃)₂O₂Cl. *Phys. Rev. B* **95**, 125121 (2017).
- [30] Zhang, T. *et al.* Magnetism and optical anisotropy in van der waals antiferromagnetic insulator CrOCl. *ACS Nano* **13**, 11353–11362 (2019).
- [31] Peng, Y. *et al.* Magnetic structure and metamagnetic transitions in the van der waals antiferromagnet CrPS₄. *Adv. Mater.* **32**, 2001200 (2020).
- [32] Zhang, M. *et al.* Metamagnetic Transitions in Few-Layer CrOCl Controlled by Magnetic Anisotropy Flipping (2021).
- [33] Szaller, D. *et al.* Coexistence of antiferromagnetism and ferrimagnetism in adjacent honeycomb layers. *arxiv* (2022).
- [34] Glauber, R. J. Time-Dependent Statistics of the Ising Model. *J. Math. Phys.* **4**, 294–307 (1963).